UHASSELT
KNOWLEDGE IN ACTION

Maastricht University

Faculty of Medicine and Life Sciences
School for Life Sciences
Master of Biomedical Sciences

Master's thesis

Nanoparticle toxicity mechanisms in human dental pulp stem cells with a focus on ferroptosis and the involvement of lipid droplets

Lisa Reynders

Thesis presented in fulfillment of the requirements for the degree of Master of Biomedical Sciences, specialization Environmental Health Sciences

SUPERVISOR :

Prof. dr. Karen SMEETS

MENTOR :

Mevrouw Anke HUYSMANS

2024
2025

Transnational University Limburg is a unique collaboration of two universities in two countries: the University of Hasselt and Maastricht University.

UHASSELT
KNOWLEDGE IN ACTION

www.uhasselt.be
Universiteit Hasselt
Campus Hasselt:
Martelarenlaan 42 | 3500 Hasselt
Campus Diepenbeek:
Agoralaan Gebouw D | 3590 Diepenbeek

Faculty of Medicine and Life Sciences
School for Life Sciences
Master of Biomedical Sciences

Master's thesis

Nanoparticle toxicity mechanisms in human dental pulp stem cells with a focus on ferroptosis and the involvement of lipid droplets

Lisa Reynders

Thesis presented in fulfillment of the requirements for the degree of Master of Biomedical Sciences, specialization Environmental Health Sciences

SUPERVISOR :

Prof. dr. Karen SMEETS

MENTOR :

Mevrouw Anke HUYSMANS

Nanoparticle toxicity mechanisms in human dental pulp stem cells with a focus on ferroptosis and the involvement of lipid droplets

Reynders Lisa[1], Anke Huysmans1[1], and Karen Smeets[1]

[1]Zoology research group, Biodiversity and Toxicology, Centre for Environmental Sciences, Hasselt University, Agoralaan Gebouw D - B-3590 Diepenbeek

Running title: *Nanoparticle-induced ferroptosis in hDPSCs*

To whom correspondence should be addressed: PI name, Tel: +32 (11) 26 83 19; Email: karen.smeets@uhasselt.be

Keywords: nanoparticle, physicochemical characteristics, developmental toxicity, human dental pulp stem cells

ABSTRACT

Humans are increasingly exposed to nanoparticles (NPs, ≤100 nm) in daily life. This growing exposure has raised concerns about potential risks to human cellular health. NPs are not only used in consumer products but are also introduced into the environment through pollution. Currently, there is a limited understanding of how the physicochemical properties of NPs affect toxicological mechanisms in (adult) developmental processes. Mesenchymal stem cells of dental pulp are capable of differentiating into various cell types, providing a valuable *in vitro* model to study how NPs may affect stem cell function and development. This study focused on and compared the effects of three widely encountered NPs of different sizes: silver (Ag, 20 nm), titanium dioxide (TiO_2, 21 nm), and polystyrene (PS, 50 nm and 1 µm) NPs, on cellular stress responses, with a focus on ferroptosis. Results indicated particle-specific and size-dependent stress responses. AgNPs induced the most pronounced ferroptotic response, marked by the differential expression of ferroptosis-related genes and increased lipid peroxidation. PSNPs triggered more moderate effects, with size-specific differences: the 1 µm particles induced stronger ferroptosis-related gene expression changes, while the 50 nm particles activated ER stress pathways. TiO_2NPs did not significantly induce ferroptosis but caused pronounced lipid droplet accumulation. Lipid droplet accumulation was observed across all NP types, likely through different mechanisms. These findings provide new insights into NP-induced cellular stress in stem cells, enhancing our understanding of NP-induced toxicity and supporting the need to consider both particle size and composition in the development of safer NPs.

INTRODUCTION

The field of nanotechnology has been growing extensively during the last two decades, with nanoparticles (NPs) being widely used in consumer products such as sunscreen and food packaging. Nanoparticles are defined as particles with one or more dimensions in the order of 100 nm or less. They possess unique properties compared to bulk materials, making them highly advantageous for various industries (1, 2). Although NPs are widely encountered, in-depth information on the relationship between the physicochemical characteristics of different NPs and their effect on human cellular health is lacking. Consequently, current risk assessment methods are inadequate, particularly regarding the effects on human developmental processes.

NPs can cross biological membranes and accumulate in various tissues, including those involved in developmental processes, raising concerns about their potential to interfere not only during early development but also in adulthood (3, 4). They have been shown to affect adult developmental processes, like the bone remodeling process, primarily through the induction of oxidative stress (5). Stem cells play a key role in these developmental processes, as they are essential for the maintenance, regeneration, and development of tissues throughout life (6). Due to their ability to self-renew and differentiate into multiple cell types, stem cells are valuable models for studying developmental toxicity. Among the most commonly studied stem cells are mesenchymal

stem cells (MSCs), which are present in adult tissues and can differentiate into multiple cell lineages, including osteoblasts, which are essential for bone formation and maintenance, and chondrocytes, which play a key role in cartilage development (7, 8, 9). Bone tissue is highly dynamic, relying on osteoblasts derived from MSCs for regeneration and structural integrity, while chondrocytes play a key role in forming and maintaining cartilage (10, 11). Disruptions in these differentiation pathways could impair tissue development and maintenance, making it crucial to understand how NPs influence these processes. Human dental pulp stem cells (hDPSCs) are MSCs present in the dental pulp of adult teeth and offer a promising tool for investigating the effects of NPs on developmental processes. These cells can be easily isolated from the pulp tissue of extracted third molars and have shown the ability to differentiate into multiple cell lineages, including chondrogenic, osteogenic, and adipogenic lineages, making them highly versatile for studying tissues undergoing active differentiation and growth (12, 13). Disruption of stem cell function can have implications for adult tissue homeostasis. *In vitro* studies have demonstrated that NPs can adversely affect stem cells by reducing cell viability, inducing apoptosis, and altering cell morphology (14, 15, 16, 17). These cellular disruptions may contribute to broader physiological consequences, such as neurodevelopmental impairments, reproductive issues, hepatotoxicity, cardiopulmonary malfunction, and immunometabolism disorders (14). Understanding these potential risks is essential for evaluating the safety of NPs and ensuring the protection of human health.

While numerous types of NPs are present in everyday environments, this study focuses on the following three types of NPs: silver (Ag), titanium dioxide (TiO_2), and polystyrene (PS) NPs.

Silver NPs (AgNPs) are metal-based NPs that are frequently used in medicine, the chemical and food industries, and agriculture because of their antibacterial properties (18, 19). These particles inhibit microbial growth by inducing reactive oxygen species (ROS), disrupting cell walls, and causing DNA damage (4). Research has indicated that AgNPs can release silver ions (Ag^+), which contribute to both their antibacterial effects and cytotoxicity (14). In addition, AgNPs and silver ions can interact with proteins and amino acids, disrupting cellular processes by affecting protein structure and function. As a result, exposure to AgNPs primarily leads to oxidative stress, DNA damage, and the induction of apoptosis (18).

TiO_2NPs are used for many applications, such as paints and cosmetic formulations. They are often added to sunscreens because they function as effective UV light filters (20). Until a few years ago, TiO_2 was used as a food additive in various food products, as identified by code E171 (Europe). However, the European Food Safety Authority (EFSA) decided in 2021 that it was no longer considered safe for consumption (EFSA, 2021). While these NPs are generally regarded as biologically inert and safe (20), studies have shown that they can disrupt cellular balance by triggering oxidative stress, which may lead to damage to cellular components, genotoxicity, and inflammation. Therefore, careful consideration of the physicochemical properties and concentrations of NPs is crucial to ensure human health safety (21, 22).

Lastly, this study includes PSNPs, which are a growing concern due to the extensive growth of global plastic production and the potential risks associated with human exposure. It is estimated that 8 million tons of plastic are released into the sea every year (23). In the environment, larger plastic items such as bottles, cartons, and straws degrade into microplastics (< 5 mm) and nanoplastics (<100 nm) through UV exposure and physical forces. This weathering process leads to particles with irregular and heterogeneous shapes (24, 25, 26). Previous research has indicated that these environmentally derived nanoplastics can enter aquatic organisms and build up through various levels of the food chain (23). However, human exposure to PSNPs is not limited to environmental sources. Nanoplastics can also be intentionally produced and added to consumer products such as cosmetics, packaging materials, and medical applications. These engineered particles are typically spherical and more uniform in size and shape, similar to the PSNPs used in this study. PS, an aromatic synthetic polymer formed through the polymerization of styrene monomers, is one of the most frequently used polymers to manufacture plastics. While PS is primarily composed of carbon and hydrogen atoms and

considered relatively inert (23, 27), studies have shown that PSNPs can enter the human body through air, food, water, and skin, after which they can accumulate in organs (23). These particles have been linked to toxic effects in the digestive, circulatory, nervous, and respiratory systems (23). At the cellular level, PSNPs have been reported to induce oxidative stress, mitochondrial dysfunction, and lysosomal damage, indicating their potential to interfere with cellular processes (28).

The cellular uptake and toxic effects of NPs are largely determined by their physical and chemical properties. Cells mostly take up NPs through endocytosis, and this process is highly dependent on the properties of the particles (22). For example, particle size is a crucial physicochemical characteristic that influences how NPs interact with biological systems. The size of NPs determines how they are distributed in the human body and how they are transported and eliminated. Smaller particles with larger surface areas to volume ratios generally tend to have greater interaction with biological tissues, leading to enhanced uptake (2, 14, 22). Furthermore, particle shape has also been determined to influence cellular uptake. NPs can be found in a variety of shapes, such as fibers, rings, tubes, oval structures, and spheres (2). Previous studies found that spherical NPs are more easily and more quickly taken up by human cells compared to rod- or fiber-shaped particles (2, 29). Additionally, the zeta potential, determined by the surface charge, plays a crucial role in maintaining the stability of NPs in dispersion (30, 31). Particles with a high zeta potential, whether positive or negative, are typically more stable and less likely to aggregate, whereas particles with low zeta potentials tend to coagulate or flocculate (31, 32). Moreover, positively charged NPs tend to exhibit greater toxicity than negatively charged ones. This is mainly due to their stronger electrostatic attraction to negatively charged phospholipids and membrane proteins, which enhances cellular uptake of the NPs (31).

As discussed before, nanotoxicity depends on the type of NPs and their physicochemical properties. However, how these properties influence developmental toxicity remains under-researched (33). ROS are thought to be major factors in the toxicity of NPs, leading to oxidative stress and inflammation (3, 34, 35). As natural byproducts of oxygen-based cellular processes, ROS are involved in various cellular activities, such as regulating cell survival, signaling, differentiation, and inflammatory responses (36, 37). They include free radicals, such as superoxide ($O_2^{\bullet-}$) and hydroxyl radical ($OH^{\bullet}$), and nonradicals, like hydrogen peroxide (H_2O_2), singlet oxygen ($^1O_2$), and hypochlorous acid (HOCl) (33, 38). While superoxide is short-lived and quickly converted to hydrogen peroxide by the enzyme superoxide dismutase (SOD), hydrogen peroxide is more stable and plays a significant role in oxidative stress management and signaling. Maintaining appropriate ROS levels is therefore crucial, and SOD enzymes are essential in preserving this cellular balance. An excessive accumulation of ROS can result in oxidative stress. This occurs when there is an imbalance between ROS production and the capacity of the biological system to neutralize these reactive molecules, triggering the activation of the cell's enzymatic and nonenzymatic antioxidant defense systems (39). At extreme levels of oxidative stress, ROS overwhelm the cell's defense mechanisms, causing mitochondrial membrane damage and dysfunction in the electron transport chain. This results in catastrophic cellular outcomes, including lipid peroxidation, protein oxidation, DNA damage, and eventually cell death via apoptosis or necrosis (40). Studies have revealed that NP toxicity is often linked to ROS generation and oxidative stress, as the physicochemical characteristics like particle size, surface charge, and NP type can catalyze the production of ROS (41, 42, 43).

Mitochondria, often described as the powerhouse of the cell, are responsible for maintaining cellular energy balance. Interestingly, they have been found to play a critical role in NP-induced toxicity (44). Their dynamic structure is governed by two critical processes, fission and fusion, which regulate mitochondrial morphology and functionality (45). Maintaining a balance between fission and fusion is crucial for preserving a healthy mitochondrial network. Mitochondrial fusion is essential in supporting the maintenance of a healthy mitochondrial network and ensuring optimal mitochondrial function by enabling the transfer of gene products between mitochondria. The mitochondrial fusion machinery relies on mitofusins 1 and 2 (Mfn1 and Mfn2), anchored in the mitochondrial outer

membrane. It also involves the GTPase optic atrophy 1 (OPA1), which is located in the mitochondrial inner membrane (46, 47). Mitochondrial fission, on the other hand, plays a key role in mitochondrial division and maintaining quality control. This process is crucial for the segregation of damaged mitochondria to mediate autophagy, apoptosis, and cell death. It is mainly mediated by fission proteins, fission 1 protein (Fis1), and mitochondrial fission factor (Mff). They assist in recruiting dynamin-related protein 1 (Drp1), a GTPase that facilitates the constriction and separation of mitochondria into smaller units (48). The structural dynamics and activity of mitochondria are key factors in the energy metabolism of the cell (49). Previous studies have shown that NPs can cause morphological changes in mitochondria, potentially disrupting fusion and fission dynamics (50, 51, 52, 53).

Mitochondria are constantly communicating with other organelles, including the endoplasmic reticulum (ER) (54). The ER is crucial for protein synthesis, transport, and folding (55). Normally, a balance exists between the amount of proteins entering the ER and its ability to fold them correctly. However, genetic and environmental factors can disrupt this balance, resulting in an accumulation of misfolded proteins, a condition known as ER stress. Once this accumulation surpasses a critical level, the unfolded protein response (UPR), an adaptive signaling pathway, is triggered to restore balance and ER function (56, 57, 58). This signaling pathway is activated by three ER sensors: inositol-requiring enzyme 1 (IRE1), double-stranded RNA-activated protein kinase R (PKR)-like ER kinase (PERK), and activating transcription factor 6 (ATF6). They activate the UPR, aiming to reduce the amount of misfolded proteins. Previous research has indicated that NPs can induce ER stress (56). For instance, studies have shown that NPs can accumulate in the ER and cause morphological changes. One notable example is TiO_2NPs, which have been shown to induce dose-dependent swelling of the ER and elevated expression of ER stress markers in mouse lungs, suggesting a potential mechanism for NP-induced pulmonary inflammation (59). When the stress induced by NPs persists, it can lead to prolonged UPR activation, eventually resulting in apoptosis. This prolonged UPR activation can significantly impair the differentiation capacity of stem cells (56, 60).

Furthermore, NPs have been found to induce ferroptosis, an iron-driven non-apoptotic cell death, characterized by intracellular iron accumulation, excessive ROS formation, and lipid peroxidation (61, 62, 63, 64, 65). Ferroptosis is mitigated by two major protective mechanisms: glutathione peroxidase 4 (GPX4) and cystine/glutamate antiporter system Xc- (66). Among these, GPX4, a key member of the glutathione peroxidase family, plays a critical role in preventing ferroptotic cell death. GPX4 uses reduced glutathione (GSH) as an electron donor to convert toxic lipid hydroperoxides (lipid-OOH) into non-toxic lipid alcohols (lipid-OH) (63, 67). On the other hand, the cystine/glutamate antiporter system Xc− plays a pivotal role by importing extracellular cystine, which is converted into GSH. This maintains the intracellular redox balance and provides the substrate needed for GPX4 activity (63, 67).

Previous studies have shown that NPs can also cause lysosomal damage and disrupt autophagy (68). Lysosomes, single-membrane vesicular organelles with an acidic lumen (pH 4.5-5.5), play a crucial role in maintaining cellular homeostasis, development, and aging. They facilitate the degradation of biomolecules such as proteins, nucleic acids, and polysaccharides, which they acquire through endocytosis and autophagy. Inside the lysosome, over 60 acidic hydrolases facilitate this degradation process. The resulting breakdown products, such as amino acids, monosaccharides, and free fatty acids, are vital for cellular energy metabolism and growth. Additionally, lysosomes contribute to intracellular signaling, nutrient transport, and ion balance by interacting with other organelles (67). Upon cellular uptake, NPs have been found to disrupt lysosome function, with the extent of damage depending on their physicochemical characteristics, such as size and morphology (67).

Autophagy is a cellular degradation process that is crucial for maintaining homeostasis. It involves the formation of double-membrane autophagosomes that fuse with lysosomes to degrade cellular components (69). A specific form of autophagy, ferritinophagy, is particularly relevant in the

context of NP toxicity. In ferritinophagy, ferritin, the main iron storage protein, is broken down, releasing iron into the cytoplasm. This free iron can participate in the Fenton reaction, generating ROS and contributing to ferroptosis. Recent evidence suggests that ferritinophagy-mediated iron release may play a key role in the induction of ferroptosis (69, 70). NP-induced autophagy has been recognized both as a contributing factor to nanotoxicity and as a protective response against NP-induced damage. However, the role of autophagy in NP-induced ferroptosis remains largely unexplored. While metallic NPs primarily induce mitochondrial stress, existing literature and preliminary laboratory findings suggest that plastic-based NPs, such as PSNPs, exert toxicity mainly through lysosomal stress (71, 72). Further research is needed to explore the contribution of this mechanism to NP-induced toxicity.

This study aims to bridge the gap in understanding how the physicochemical properties of different NPs influence cellular toxicity. Previous studies often focused on the toxic effects induced by NPs, while the physicochemical properties were often overlooked. By characterizing and comparing AgNPs, TiO_2NPs, and PSNPs and investigating their effects on hDPSCs, this research provides valuable insights into their cellular interactions, oxidative stress responses, mitochondrial dynamics, lysosomal stress, and potential links to ferroptosis. The findings contribute to a deeper understanding of NP-induced cellular toxicity in stem cells, an important *in vitro* model for studying developmental toxicity, aiding in risk assessment and the development of safer nanomaterials for human exposure.

EXPERIMENTAL PROCEDURES

Cell culture – hDPSCs were provided by the Biomedical Research Institute (BIOMED, Hasselt University, Belgium) and cultured in culture flasks containing minimum essential medium alpha culture medium (α-MEM, VWR, Oud-Heverlee, Belgium), supplemented with 10% heat-inactivated fetal bovine serum (FBS, Sigma-Aldrich, Darmstadt, Germany), 1% penicillin/streptomycin (Pen/Strep, Gibco, Fisher Scientific, Brussels, Belgium), and 1% L-glutamine (VWR, Oud-Heverlee, Belgium). Cells were maintained at 37 °C in an incubator with a 5% CO_2 atmosphere, with the medium refreshed every other day. Cells were passaged at 70-90% confluence. Therefore, they were washed twice with phosphate-buffered saline (PBS, without Ca^{2+} or Mg^{2+}, VWR, Oud-Heverlee, Belgium). Subsequently, 0.05% trypsin-EDTA (Gibco, Fisher Scientific, Brussels, Belgium) was incubated for 5 minutes at 37 °C and 5% CO_2. The enzymatic activity of trypsin-EDTA was stopped by adding at least three volumes of complete cell medium relative to the volume of trypsin used. Cells were pelleted by centrifuging at 300 g for 5 minutes and resuspended in complete medium.

Materials – Three types of commercially available NPs were purchased. Spherical polyvinylpyrrolidone (PVP)-AgNPs of 20 nm (US Research Nanomaterials Inc., Houston, Texas, USA) and spherical TiO_2NPs of 21 nm (Sigma-Aldrich, Darmstadt, Germany) were obtained. Additionally, red fluorescent (RF) and non-fluorescent (NF) PSNPs, functionalized with carboxylic surface groups (-COOH), were purchased with two particle diameters: 50 nm (PS50NF and PS50RF) and 1 µm (PS01NF and PS01RF) (Magsphere Inc., Pasadena, California, USA). NP stocks (1 mg/mL) were prepared in autoclaved and filtered Milli-Q water.

Physicochemical characterization of nanoparticles – NP morphology and size were determined using Scanning Transmission Electron Microscopy (STEM). First, particle suspensions were prepared in water. Then, pioloform-coated mesh copper grids were treated with Alcian blue for 10 minutes to render a positive surface charge, followed by five washes with water. To prepare STEM samples, the treated grids were placed onto a droplet of the particle suspension for 10 minutes. Following incubation, the grid was carefully lifted from the droplet and gently dried with filter paper. STEM-EDX imaging was performed using the Talos F200S G2 transmission electron microscope, equipped with an HAADF detector and Super-X EDS detector. Analyses were performed for at least 300 particles using ImageJ (1.54g; Java 1.8.0_345) software to determine the particle minimum Feret diameter and aspect ratio.

Gene expression analysis – To measure changes in gene expression of selected genes, a quantitative polymerase chain reaction (qPCR)

was performed. DPSCs were seeded at 4 x 10^4 cells/12-well and grown to 50% confluence. After exposure to 10 µg/mL AgNPs and TiO_2NPs, and 10 and 100 µg/mL PS50NF and PS01NF for 16, 24, and 48 hours in α-MEM, the cells were washed twice with Dulbecco's phosphate-buffered saline (DPBS, $+Ca^{2+}$, $+Mg^{2+}$, VWR, Oud-Heverlee, Belgium). Then, the cells were lysed in plates with cold lysis buffer and stored at -80 °C for further processing. Total RNA was extracted from the cells using a phenol/chloroform extraction. RNA concentration and purity were measured using a nanodrop ND-1000 spectrophotometer (Isogen Life Science, Utrecht, Netherlands). After TurboDNase (Turbo DNA-free kit, Invitrogen, Fisher Scientific, Brussels, Belgium) treatment to remove genomic DNA, RNA was reverse transcribed using the Goscript reverse transcription system (Promega, Madison, Wisconsin, USA). All qPCR reactions were performed using the QuantStudio 3 qPCR machine (Applied Biosystems, Thermo Fisher Scientific, Brussels, Belgium). Each reaction contained cDNA and master mix containing Fast SYBR Green OCR Master mix (Applied Biosystems, Thermo Fisher Scientific, Brussels, Belgium), and forward and reverse primers (Supplementary Table 1). The reaction was performed using qPCR cycling conditions: initial denaturation at 95 °C for 20s, followed by 40 cycles of denaturation at 95 °C for 1s and annealing/extension at 60 °C for 20s. The primer sequences for the studied genes were based on existing literature. Fold change was calculated from Ct-values and normalized for four reference genes. Relative quantification of gene expression was performed following the standard $2^{-\Delta\Delta Ct}$ method.

Lipid droplets staining - An Oil Red O staining (ORO, Sigma-Aldrich, Darmstadt, Germany) was performed to visualize intracellular lipid droplets. Cells were seeded on glass coverslips at 2 x 10^4 cells/24-well and cultured for 2 days. After exposure to 1 and 10 µg/mL AgNPs and 10 and 100 µg/mL TiO_2NPs and PS50RF for 8, 24, and 48 hours, cells were washed three times with warm DPBS and then fixed in 4% paraformaldehyde (Sigma Aldrich, Darmstadt, Germany), followed by another three washes with DPBS. A stock solution of Oil Red O was prepared by dissolving 0.5 g of Oil Red O powder in 100 mL of isopropanol (VWR, Oud-Heverlee, Belgium). For the working solution, 6 mL of the stock solution was mixed with 4 mL of distilled water. Next, cells were stained with 200 µL of freshly prepared and filtered ORO solution for 10 minutes at room temperature (RT), washed three times with PBS, and nuclei were counterstained with DAPI for 15 minutes. After three final washes in PBS, coverslips were mounted with Prolong Gold Antifade mounting medium (Invitrogen, Thermo Fisher Scientific, Brussels, Belgium) and imaged using confocal laser scanning microscopy (CLSM, LSM 900, Zeiss, Zaventem, Belgium) at emission wavelengths of 465 and 636 nm at 40x magnification to visualize the nucleus and the lipid droplets, respectively. Finally, a quantitative analysis was conducted to assess the lipid droplet count, as well as the lipid droplet area per cell. Approximately 35 cells were analyzed per condition, with two technical replicates for each condition.

Malondialdehyde (MDA) staining - An immunofluorescent stain was used to visualize MDA, a byproduct of lipid peroxidation, which is one of the hallmarks of ferroptosis. Briefly, DPSCs were seeded at 1 x 10^4 cells/24-well and cultured for 2 days. Cells were then exposed to 10 µg/mL AgNPs and 10 and 100 µg/mL of the TiO_2NPs for 48 hours. As a positive control for lipid peroxidation, cells were treated with 250 µM hydrogen peroxide (H_2O_2, Thermo Fisher Scientific, Brussels, Belgium) for 30 minutes before fixation. After exposure, cells were washed three times with warm DPBS and fixed in 4% paraformaldehyde for 15 minutes at RT. Following three washes with DPBS, cells were permeabilized using 0.1% Triton X-100 (Sigma-Aldrich, Darmstadt, Germany) for 15 min at RT, then washed again three times with PBS. To block nonspecific binding of the antibody, cells were incubated with 2% Bovine Serum Albumin (BSA, Sigma Aldrich, Darmstadt, Germany) in PBS for 60 minutes at RT. They were then incubated with the primary MDA antibody (11E3, Invitrogen, Thermo Fisher Scientific, Brussels, Belgium), diluted 1/100 in 0.1% BSA, for three hours at RT. After incubation, the primary antibody was removed by washing three times with PBS. A 1/200 dilution of the secondary Alexa Fluor 488 goat anti-mouse (Invitrogen, Thermo Fisher Scientific, Brussels, Belgium) was made in 0.1% BSA and incubated for 45 minutes at RT.

The cells were again washed three times with PBS and incubated with DAPI for 15 minutes at RT at a dilution of 1/1000 to counterstain the nuclei. Finally, the cells were washed three times with PBS, mounted with Prolong Gold Antifade mounting medium, and imaged using CLSM at emission wavelengths of 465 and 517 nm at 40x magnification to visualize the nucleus and MDA, respectively. Finally, a quantitative analysis was conducted by measuring fluorescence intensity with ImageJ (1.54g; Java 1.8.0_345). Approximately 25 cells were analyzed per condition, with two technical replicates for each condition.

TEM images for qualitative analysis - A qualitative TEM analysis was performed to compare possible alterations in cellular ultrastructures between conditions. Cells were seeded at 1.5 x 10^4 cells/24-well. The next day, they were exposed to 100 µg/ml of the PS01NF particles and 10 µg/ml of the AgNPs and TiO_2NPs. After a 48-hour exposure period, the cells were washed thrice with warm DPBS, fixed in 2% glutaraldehyde (Sigma Aldrich, Darmstadt, Germany) buffered with 0.05 M sodium cacodylate, and embedded in epoxy resin. Then, 70 nm ultra-thin sections of cell samples were prepared. The cellular ultrastructures were observed and photographed with the TEM (JEM-1400 Flash (JEOL, Tokyo, Japan)), equipped with a 20 MP XAROSA CMOS camera (EMSIS, Münster, Germany), operating at 80 kV.

Statistical analysis – R software, version 2024.12.0, was used to perform statistical analysis. The normality and homoscedasticity of the data were verified using the Shapiro-Wilk test and Levene test, respectively. If the data were normally distributed, a one-way ANOVA was performed to evaluate differences across different conditions, followed by a post-hoc Dunnett's test to identify specific group differences. In case normality was violated, the non-parametric test, Kruskal-Wallis, was performed, followed by a post-hoc Dunn test. A p-value < 0.05 was considered to be statistically significant.

RESULTS

NP characterization – Image analysis of the STEM images provided size and shape information on the NPs (Table 1 & Figure 1). The minimum Feret diameter for the PVP-AgNPs was measured at 22.915 ± 12.201 nm, with an aspect ratio of 1.375 ± 0.3019, indicating a spherical shape. Similarly, the TiO_2NPs showed a minimum Feret diameter of 19.210 ± 7.225 nm and an aspect ratio of 1.221 ± 0.180, also indicating sphericity. Furthermore, the PS50NF particles exhibited a minimum Feret diameter of 33.889 ± 11.881 nm and an aspect ratio of 1.026 ± 0.025, also indicating a spherical shape. The PS01NF particles showed a minimum Feret diameter of 956.044 ± 123.501 nm with an aspect ratio of 1.0830 ± 0.541, again indicating sphericity. The red-fluorescent counterparts of these particles exhibited similar characteristics. PS50RF particles showed a minimum Feret diameter of 29.282 ± 8.830 nm and an aspect ratio of 1.035 ± 0.038, while PS01RF particles measured 951.710 ± 100.724 nm with an aspect ratio of 1.073 ± 0.063. These aspect ratios are again close to 1, confirming a spherical shape.

Table 1 – Physical characteristics of NPs based on STEM

	Manufacturer	STEM	STEM
NP	Particle size (nm)	Min Feret diameter (nm)	Aspect ratio
PVP-Ag	20	22.915 ±12.201	1.375 ± 0.3019
TiO_2	21	19.210 ± 7.225	1.221 ± 0.180
PS50NF	50	33.889 ± 11.881	1.026 ± 0.025
PS50RF	50	29.282 ± 8.830	1.035 ± 0.038
PS01NF	1 µm	956.044 ± 123.501	1.0830 ± 0.541
PS01RF	1 µm	951.710 ± 100.724	1.073 ± 0.063

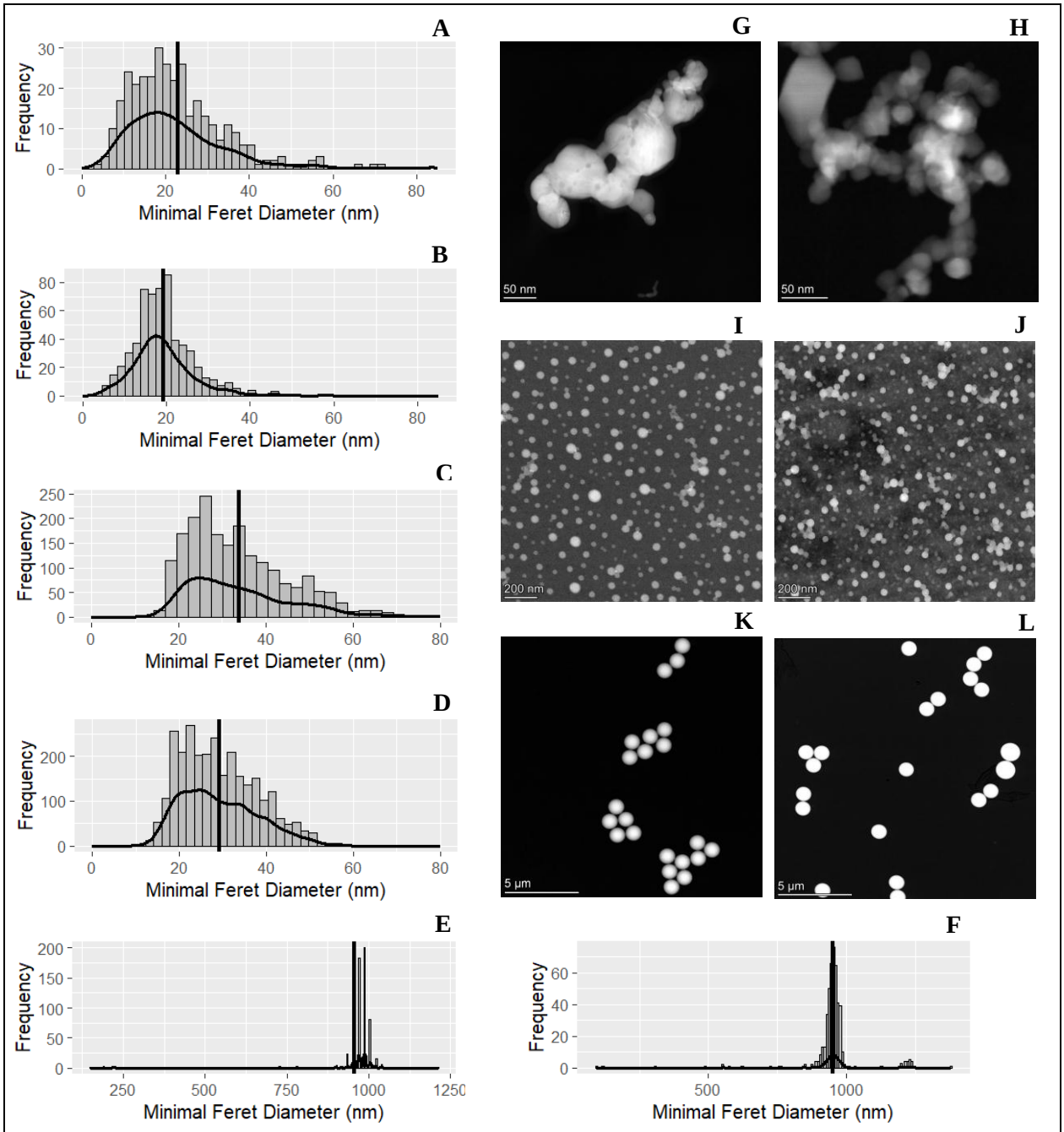

Figure 1 – Size distribution of NPs. ImageJ software was used to determine particle minimum Feret diameter. (A) AgNPs, (B) TiO_2NPs, (C) PS50NF, (D) PS50RF, (E) PS01NF, (F) PS01RF. Bars represent the frequency (n) on the y-axis. Images of (G) AgNPs, 250kx, (H) TiO_2NPs, 360kx, (I) PS50NF, 62kx, (J) PS50RF, 62kx, (K) PS01NF, 5600x, (L) PS01RF, 5600x were acquired by STEM.

Effects of NPs on gene expression in cellular processes in DPSCs – Gene expression levels of selected genes were measured after 16 and 48 hours of exposure to gain insights into the cellular response of DPSCs to the studied NPs. While several statistically significant differences were observed between exposed conditions and the control, it is important to note that these often reflect relatively modest changes in expression levels and should be interpreted with caution regarding their biological relevance. Based on these initial findings, genes were selected to study the gene expression levels after 24 hours of exposure. The results are visualized in heatmaps (Figure 2), where gene expression levels relative to the control are color-coded and statistical significance is indicated (* for $p < 0.05$, considered significant, ° for $p < 0.1$, considered a trend).

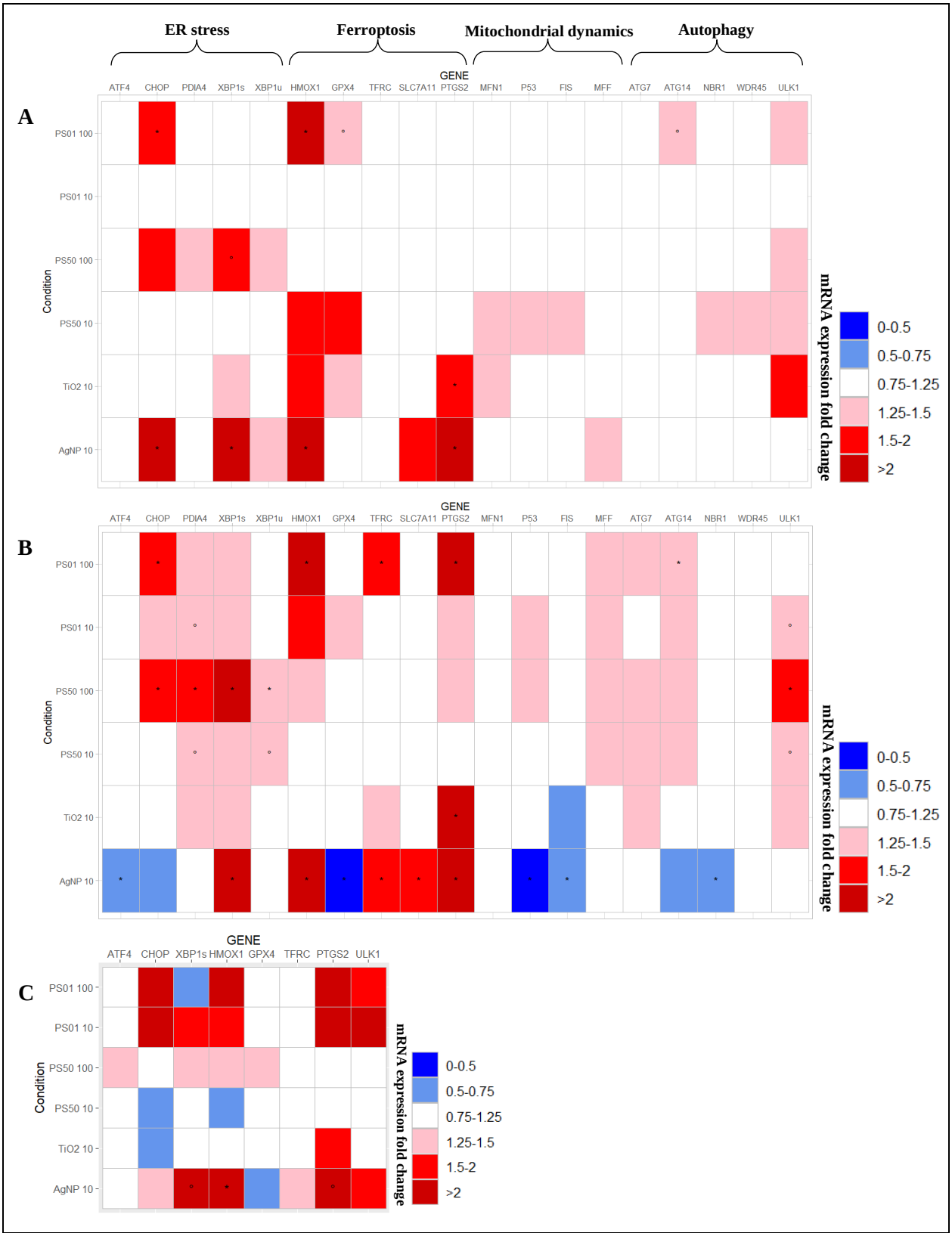

Figure 2 – Heatmap of the gene expression level fold changes after (A) 16, (B) 48, and (C) 24 hours of exposure to 10 µg/mL AgNPs, TiO_2NPs, PS50NF, and PS01NF, and 100 µg/mL PS50NF and PS01NF. Gene expression is shown as fold change relative to control and color-coded by expression level. The fold changes of genes were normalized using four reference genes (GAPDH, HPRT1, TBP, RPLP0). n = 4-7 from one experiment. Statistical significance is indicated by symbols: ° $p < 0.1$, * $p < 0.05$. Genes are grouped by cellular process, as indicated by square brackets above the heatmap. These categories include ER stress, ferroptosis, mitochondrial dynamics, and autophagy.

After 16 hours of exposure, AgNP exposure caused significant upregulation of PTGS2, HMOX1, XBP1s, and CHOP. TiO_2NPs also induced a significant increase in PTGS2 expression. For the highest concentration of the 1 µm-sized PSNPs, CHOP and HMOX1 were significantly upregulated, with GPX4 and ATG14 showing trends toward increased expression. Most autophagy- and mitochondrial dynamics-related genes remained unaffected at this early time point.

Prolonged exposure of 48 hours led to a more diverse transcriptional profile with several genes showing significant up- or downregulation depending on the NP type. In AgNP-exposed cells, PTGS2, SLC7A11, TFRC, HMOX1, and XBP1s were significantly upregulated, while GPX4, ATF4, NBR1, FIS, and P53 were significantly downregulated. TiO_2NPs again caused significant upregulation of PTGS2, although changes in other genes were limited. Exposure to the lowest concentration of the 50 nm-sized PSNPs led to

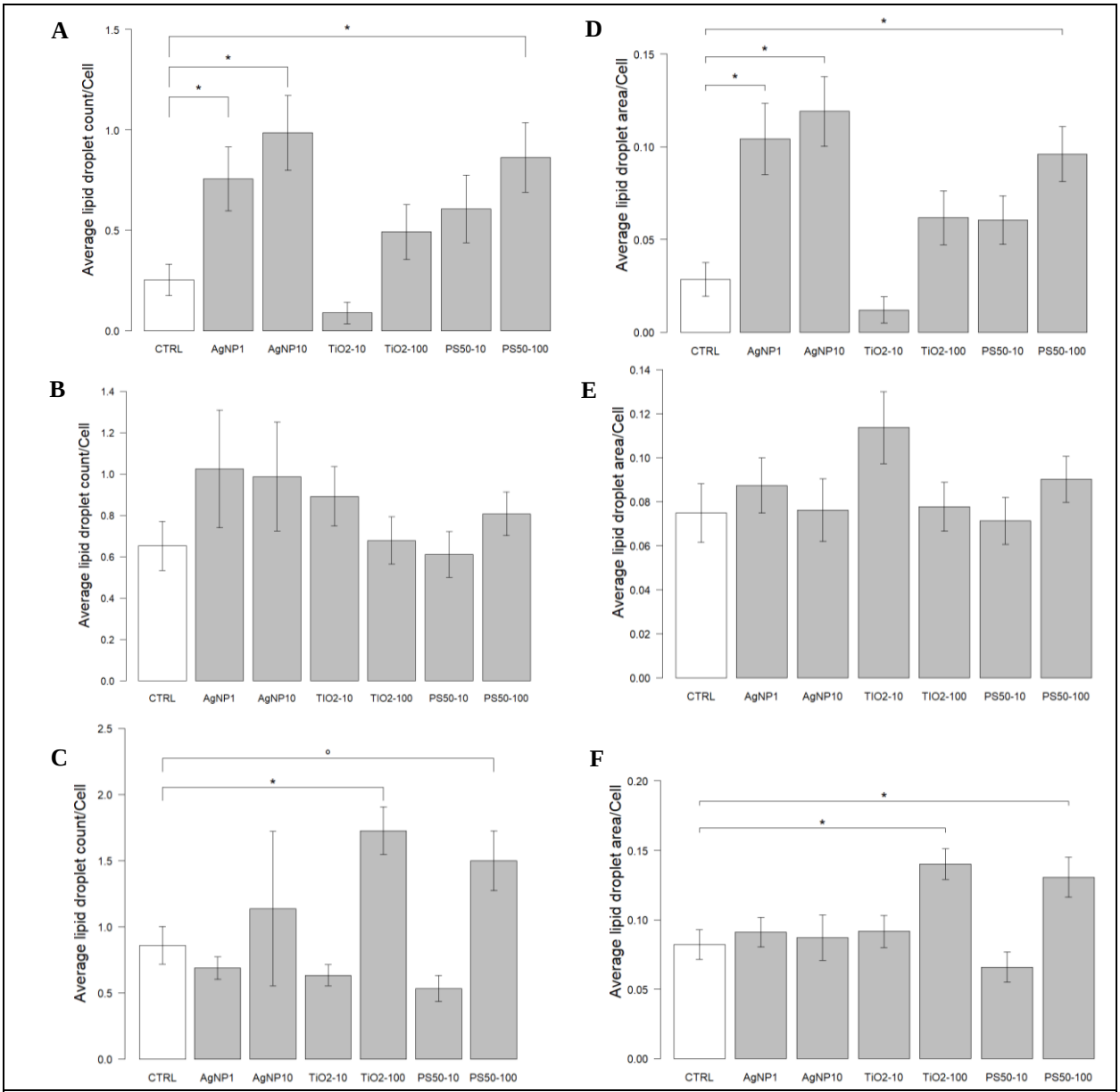

Figure 3 – Oil Red O staining after exposure to 1 µg/mL AgNPs, 10 µg/mL AgNPs, TiO_2NPs, and PS50RF and 100 µg/mL TiO_2NPs and PS50RF for 8, 24, and 48 hours. (A-C) Average lipid droplet count per cell following NP exposure for (A) 8, (B) 24, and (C) 48 hours. Bars represent mean ± standard error of lipid droplet number per cell. (D-F) Average lipid droplet area per cell following NP exposure for (D) 8, (E) 24, and (F) 48 hours. Bars represent mean ± standard error of lipid droplet area per cell. Statistical significance is indicated by symbols: ° $p < 0.1$, * $p < 0.05$.

a mild upregulation of XBP1u and PDIA4, whereas the highest concentration induced significant upregulation of CHOP, PDIA4, XBP1s, XBP1u, and ULK1.

For the highest concentration of the 1 µm-sized PSNPs, significant upregulation of PTGS2, TRFC, HMOX1, CHOP, and ATG14 was observed. In contrast, the lowest concentration of the 1 µm-sized PSNPs showed only trends toward upregulation for PDIA4 and ULK1. Gene expression changes at 24 hours after NP exposure showed intermediate patterns compared to the 16-hour and 48-hour time points. AgNPs induced a significant upregulation of HMOX1, along with trends toward increased expression of XBP1s and PTGS2. No statistically significant gene expression changes were detected in response to TiO_2NPs or PSNPs at this time point.

Effects of NPs on lipid droplet count and area – To investigate lipid droplet formation over time following NP exposure, an ORO staining was performed. The number and total area of lipid droplets per cell were quantified after 8, 24, and 48 hours of NP exposure.
After 8 hours of exposure (Figure 3A), a significant increase in the number of lipid droplets per cell was observed in cells exposed to AgNPs at both 1 µg/mL (0.76 ± 0.16, $p = 0.0095$), and 10 µg/mL (0.99 ± 0.19, $p = 0.00097$), as well as PSNPs (50 nm) at 100 µg/mL (0.86 ± 0.17, $p = 0.0082$), compared to the control group (0.25 ± 0.078). Other conditions showed no significant effect. These effects were not seen at the 24-hour timepoint, where no statistically significant differences in lipid droplet count were found across any conditions (Figure 3B). However, after 48 hours (Figure 3C), exposure to TiO_2NPs at 100 µg/mL resulted in a significantly increased lipid droplet number (1.73 ± 0.18, $p = 0.00013$). PSNPs (50 nm) at 100 µg/mL showed a borderline significant increase (1.50 ± 0.22, $p = 0.053$) compared to the control (0.86 ± 0.14). No other treatments resulted in significant alterations at this stage.
A similar pattern was observed for lipid droplet area. Significant increases were observed at 8 hours (Figure 3D) in cells exposed to AgNPs at 1 µg/mL (0.10 ± 0.019, $p = 0.00381$), and 10 µg/mL (0.12 ± 0.019, $p = 0.00039$), and PSNPs at 100 µg/mL (0.096 ± 0.015, $p = 0.00333$), compared to the control (0.029 ± 0.009). No significant differences were found for other conditions at this time point. Furthermore, no significant differences were observed across conditions after 24 hours of NP exposure (Figure 3E). After 48 hours (Figure 3F), a significant increase in lipid droplet area was observed for TiO_2NPs at 100 µg/mL (0.14 ± 0.011, $p = 0.00047$) and for PSNPs at 100 µg/mL (0.13 ± 0.015, $p = 0.03$), compared to the control (0.082 ± 0.011). Other conditions did not show significant differences.

Lipid peroxidation levels after NP exposure – MDA fluorescence intensity was expressed relative to the negative control (set at 1) and showed differences in levels of lipid peroxidation between the experimental groups (Figure 4). Exposure to AgNPs (10 µg/mL) resulted in a marked increase in MDA staining, with an average relative intensity of 1.38 ± 0.071, which was significantly higher than the negative control ($p = 0.00066$). A similar pattern was observed in the positive control group, which showed the highest overall relative intensity of 1.46 ± 0.12, also significantly elevated compared to the negative control ($p = 0.00603$), thereby confirming the effectiveness of the staining. Interestingly, cells exposed to TiO_2NPs at 10 µg/mL exhibited a reduction in relative MDA intensity (0.85 ± 0.033) that was significantly lower than

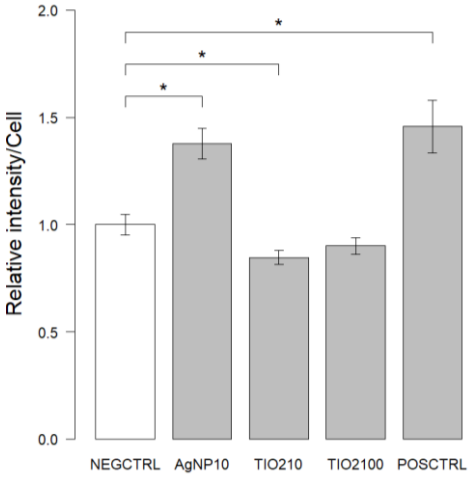

Figure 4 – Quantification of MDA levels after exposure to 10 µg/mL AgNPs and TiO_2NPs, and 100 µg/mL TiO_2NPs for 48 hours. Bars represent mean MDA fluorescence intensity ± standard error relative to the negative control. Statistical significance is indicated by symbols: ° $p < 0.1$, * $p < 0.05$.

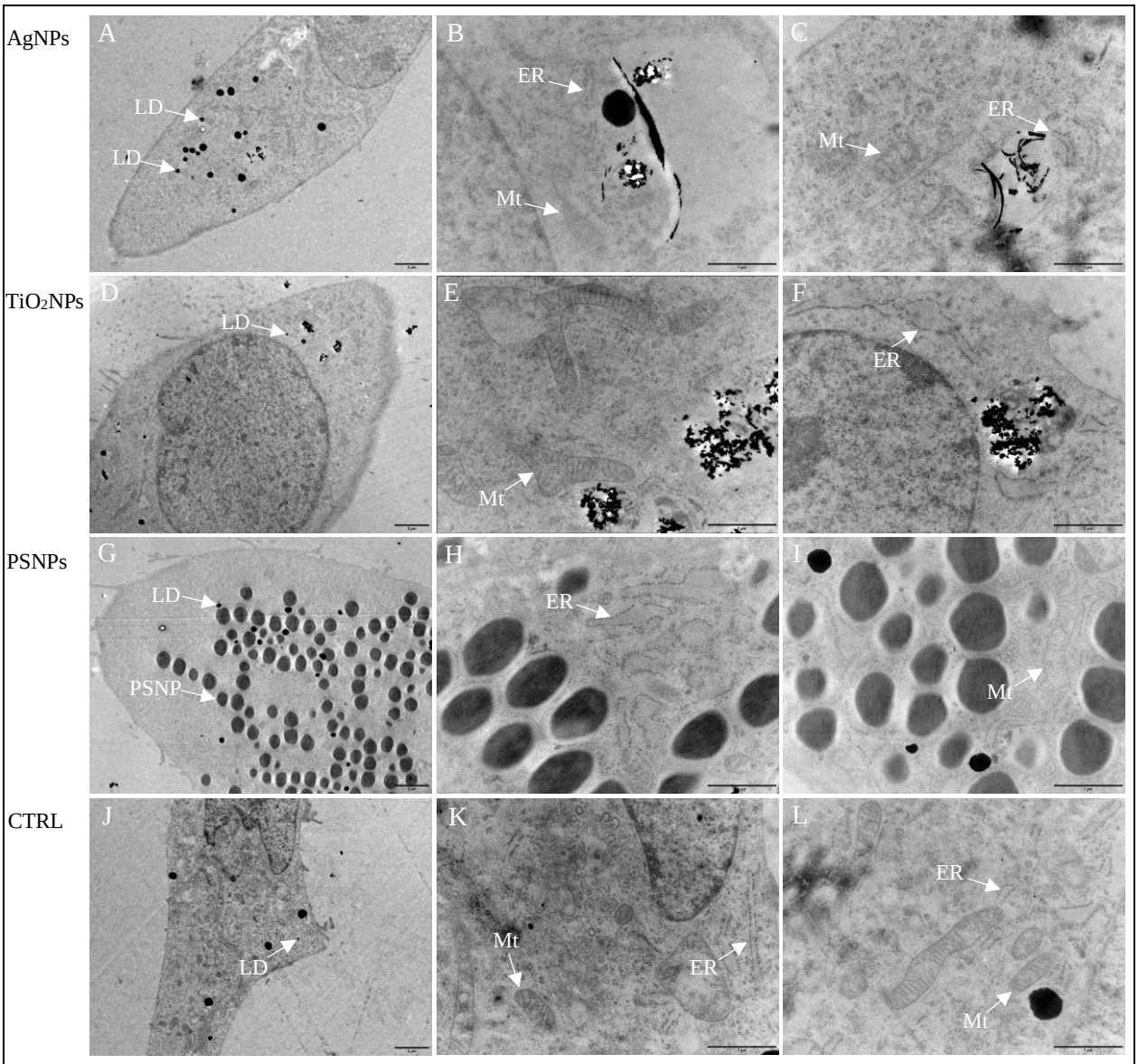

Figure 5 – Qualitative TEM analysis of cellular ultrastructures after exposure to 10 µg/ml of AgNPs and TiO_2NPs, and 100 µg/ml of PS01NF for 48 hours. LD: lipid droplet, ER: endoplasmic reticulum, Mt: mitochondria, CTRL: negative control. (A) TEM image: AgNPs, 2500x (B,C) TEM image: AgNPs, 10000x (D) TEM image: TiO_2NPs, 2500x (E,F) TEM image: TiO_2NPs, 10000x (G) TEM image: PSNPs, 2500x (H,I) TEM image: PSNPs, 10000x (J) TEM image CTRL, 2500x (K,L) TEM image: CTRL, 10000x.

the negative control ($p = 0.048$). Exposure to the higher dose of TiO_2NPs led to a slightly decreased relative intensity of 0.90 ± 0.038, but this difference was not statistically significant.

Qualitative TEM analysis - TEM images showed well-preserved cellular and organelle structures across all conditions, indicating that no major cytotoxic damage was visible at the ultrastructural level. In PS01NF-exposed cells (Figure 5G-I), the ER appeared dilated. Furthermore, PSNPs were most commonly observed within individual vesicles. Mitochondria and lysosomes seemed to maintain a normal appearance. Also, an increased number of lipid droplets could be observed compared to control cells (Figure 5 J-K).

Cells exposed to AgNPs (Figure 5A-C) similarly showed NPs enclosed within intracellular vesicles, with particles often forming agglomerates. In parallel with the ORO results, an elevated number of lipid droplets could be observed. No notable morphological

abnormalities were detected in the mitochondria, ER, or lysosomes.
In contrast, TiO_2NP-exposed cells exhibited more pronounced ultrastructural changes (Figure 5D-F). Mitochondria seemed to appear elongated and display increased branching, while the ER showed a dilated appearance. NPs were generally observed in vesicles, often forming agglomerates. Despite these changes, no clear increase in lipid droplets was observed compared to the control cells, and lysosomal structures appeared largely unaltered.

DISCUSSION

The increasing presence of NPs in our daily environment is raising concerns about their interference with essential developmental processes, not only during early development, but also during adulthood. This study provides insights into the effects of three different NPs on cellular stress responses in hDPSCs, with an emphasis on possible ferroptosis and lipid droplet dynamics. The findings of this study demonstrate that AgNPs showed the strongest tendency toward inducing ferroptosis, marked by the differential expression of ferroptosis-related genes and increased lipid peroxidation. Additionally, lipid droplet accumulation was observed. Secondly, PSNPs also triggered the differential expression of ferroptosis-related genes, together with an increased lipid droplet accumulation, particularly at higher concentrations and longer exposure times. Thirdly, TiO_2NPS did not strongly activate ferroptotic pathways, but caused significant lipid droplet accumulation at 48 hours of exposure. However, these findings do not exclude the potential involvement of ferroptosis in the toxicity of TiO_2NPs, warranting further investigation.

The most pronounced ferroptotic response was observed in the AgNP-treated cells. Gene expression analysis revealed a time-dependent pattern. After 16 hours of exposure, only PTGS2 and HMOX1, markers of ferroptosis, were significantly upregulated in response to AgNP exposure. Interestingly, at 24 hours of exposure, a more defined ferroptotic profile began to emerge, marked by significantly increased expression of PTGS2 and HMOX1. This pattern intensified after 48 hours of exposure, where AgNPs induced the differential gene expression for a broader set of ferroptosis-related genes, including PTGS2, HMOX1, SLC7A11, and TFRC, alongside downregulation of GPX4. Notably, PTGS2 and HMOX1 showed a particularly strong upregulation, with fold changes of 5.5 and 7.4, respectively. The downregulation of GPX4 is important as this is a key regulator of ferroptosis that converts toxic lipid hydroperoxides (lipid-OOH) into non-toxic lipid alcohols (61, 73). Supporting these gene expression results, the MDA staining results confirmed that AgNPs significantly increased lipid peroxidation levels. MDA, a byproduct of lipid peroxidation and a commonly used biomarker of ferroptosis, accumulates when oxidants such as free radicals attack the polyunsaturated fatty acids (PUFAs) in lipid membranes, leading to oxidative membrane damage (74). The observed GPX4 downregulation and elevated MDA levels align with studies by Zheng et al (2023) and Zhai et al. (2024), which also reported GPX4 downregulation and enhanced lipid peroxidation (61, 73). Additionally, Zhai et al. (2024) observed that AgNP-treated neuron cells induced shrunken mitochondria with fewer cristae, which is typical for ferroptosis (73). This is not in line with the mitochondrial morphology observed in our study, where the AgNP-treated cells showed no notable different morphology compared to the non-exposed cells. However, it is important to note that this may be due to the qualitative nature and limited sample size of our TEM analysis. Therefore, future studies could apply both stereological and morphometric methods to quantitatively assess ultrastructural alterations. While morphometry involves direct two-dimensional measurements, stereology allows for three-dimensional measurements, based on the analysis of two-dimensional cut sections (75, 76). Additionally, Zheng et al. (2023) highlighted that smaller AgNPs were more effective in inducing ferroptosis, suggesting a size-dependent effect (61). Although our study only included one AgNP size, these findings highlight the need for future research to explore potential size-dependent effects.

Furthermore, the results of the ORO staining revealed an early and significant accumulation of lipid droplets in response to AgNPs at both concentrations. These NPs significantly increased both the number of lipid droplets and the total lipid droplet area per cell. This observation supports our hypothesis that lipid droplets serve as a protective mechanism

against lipid peroxidation. This hypothesis was also confirmed by Bailey et al. (2015). They found that lipid droplets in glial cells protect Drosophila neural stem cells from lipid peroxidation by sequestering PUFAs away from membranes (77). On the other hand, when lipid droplets are broken down too abruptly, PUFAs can be released in large quantities, increasing the risk of oxidative stress and subsequent lipid peroxidation (78). Additionally, it has been shown that lipid droplet accumulation is induced during the early phase of ferroptosis but declines at later stages. In the context of this study, early lipid droplet formation may reflect an early protective response to counteract NP-induced oxidative stress (78). This could also explain our results, where we observed that lipid droplet numbers and area peaked after 8 hours of exposure and became less prominent after longer AgNP exposure.

In addition to the ferroptosis-related gene expression changes, AgNP exposure also affected genes associated with ER stress. After 16 hours of exposure, XBP1s and CHOP, two important genes involved in the UPR, were significantly upregulated. XBP1s remained upregulated after 24 and 48 hours of AgNP exposure. XBP1s is the spliced and transcriptionally active form of XBP1, generated via activation of IRE1, one of the three major ER stress sensors. Once spliced, XBP1s translocates to the nucleus, where it regulates the UPR to restore ER homeostasis (79). ATF4, another important transcription factor in ER stress signaling, was significantly downregulated after 48 hours of exposure. This was not expected, given that ATF4 is typically upregulated during ER stress. However, the observed fold change was only 0.55, indicating that this result, while statistically significant, reflects only a subtle biological effect.

TiO_2NPs presented a more ambiguous toxicity profile. Among the ferroptosis-related genes, only PTGS2, a gene that is typically upregulated during ferroptosis and responsible for activating inflammatory responses, was significantly upregulated after 16 hours and 48 hours of exposure (80). While only PTGS2 was significantly upregulated, MDA staining at the lowest concentration led to a significant decrease in MDA levels, indicating reduced lipid peroxidation compared to the control. This contrasts with previous findings by Huang et al. (2025), who reported that TiO_2NPs (30 nm) could increase MDA levels in a concentration-dependent way after 24 hours of exposure in human umbilical vein endothelial cells (HUVECs). Additionally, they found a reduced protein expression of GPX4 (81). A possible explanation for these discrepancies is that MDA analysis in our study was limited to the 48-hour time point, possibly missing earlier cellular responses. Additionally, the small sample size may have limited the detection of subtle effects. In the qualitative TEM analysis, the TiO_2NP-exposed cells did show ultrastructural changes as mitochondria appeared elongated and the ER showed a dilated appearance. However, given the qualitative nature of this analysis, these observations should be interpreted with caution. Interestingly, despite the absence of a defined ferroptotic gene expression profile and reduced MDA levels, TiO_2NPs induced the most pronounced lipid droplet accumulation at 48 hours of exposure, reflected by increased lipid droplet number and total lipid droplet area. This unexpected finding may point toward alternative mechanisms, such as ER stress or general oxidative imbalance. TiO_2NPs have previously been shown to cause ER swelling and activate the unfolded protein response (59). As discussed earlier, lipid droplet formation is a protective mechanism against lipid peroxidation during ferroptosis. However, studies have shown that lipid droplets also protect against ER stress by sequestering misfolded proteins, rebalancing ER lipid homeostasis, and regulating other stress responses, such as autophagy (82). Furthermore, in a review of Manzoor et al. (2024), the authors highlight that TiO_2NP-induced toxicity remains under-researched (21). Some studies find no indications of toxicity, while others point out their ability to induce oxidative stress, genotoxicity, and immunotoxicity. An important factor contributing to these differences in TiO_2NP toxicity may be particle size. In the study of Xiong et al. (2013), they found an inverse relationship between particle size and phototoxicity (83). Cells exposed to 10 nm TiO_2NPs showed significantly higher mortality and generated more mitochondrial superoxide after UV photoactivation compared to those treated with larger particles (20 and 100 nm) (83). This can be explained by the fact that smaller particles have a higher surface area to volume ratio, and they tend to have a greater

interaction with biological tissues. These findings highlight the influence of physicochemical properties on biological effects. Despite the similar sizes of AgNPs and TiO_2NPs in our study, their different core compositions likely account for their different toxicity profiles. This is mainly because AgNPs can release silver ions, making them highly reactive, whereas TiO_2NPs are often described as biologically inert (18, 20).

PSNPs elicited a more subtle ferroptotic response. Although MDA staining was not performed for PSNPs in this study, the highest concentration of the 1 µm particles showed some gene expression changes in ferroptosis-related genes. After 16 hours of exposure, the 1 µm PSNPs induced a significant upregulation of HMOX1. After 48 hours of exposure, the ferroptotic response became more pronounced. The highest concentration of the 1 µm-sized PSNPs showed a significant upregulation of PTGS2, TFRC, and HMOX1, together with a significant upregulation of the ER stress-related gene CHOP. For the 50 nm-sized PSNPs, no changes were observed in the gene expression of ferroptosis-related genes. However, ER stress-related genes did show some notable gene expression changes. A significant upregulation of XBP1u, XBP1s, PDIA4, and CHOP was observed. These results align partly with a study by Wu et al. (2024), where two sizes of PS-MNPs (10 µm and 20 nm) were investigated. They observed that only PSNPs of 20 nm induced toxicity in B2B cells by activating ER stress pathways. On the other hand, they did find increased levels of MDA after exposure to the 20 nm-sized PSNPs. Additionally, they reported that after exposure to PSNPs, GPX4 levels decreased in a dose-dependent manner. Lastly, they found morphological changes indicating ferroptosis, including swelling of mitochondria and decreased mitochondrial cristae (84). While they describe mitochondrial swelling as indicative of ferroptosis, most studies contradict this and associate ferroptosis with mitochondrial membrane shrinkage (85). Our findings indicated only a subtle tendency toward ferroptosis induction at the particle sizes tested. This may be attributed to the larger particle sizes used in our study compared to the smaller 20 nm PSNPs used in the study of Wu et al. (2024) (84). However, in the lipid droplet experiment, exposure to PSNPs (50 nm, 100 µg/mL) did cause a significant increase in both lipid droplet number and total droplet area per cell after 8 hours of exposure. This effect persisted after 48 hours of exposure, with the total lipid droplet area remaining statistically significantly elevated compared to the control. As discussed earlier, this could be an indication of ER stress.

Ferroptosis is characterized by intracellular iron accumulation. To obtain a more complete understanding of ferroptosis, a Ferro Orange staining protocol was optimized in this study to detect intracellular ferrous iron (Fe^{2+}). Although this staining was not applied within the current experimental timeframe, it is included in the supplementary information and is ready to be used in future experiments. Zhai et al. (2024) also used this Ferro orange staining and emphasized the critical role of intracellular iron accumulation in ferroptosis (73). Therefore, the optimized protocol developed in this study will represent a valuable addition in future experiments, as excessive iron accumulation is a hallmark of ferroptosis.

In this study, we also included autophagy-related and mitochondrial dynamics-related genes. However, limited attention has been given to these results as there were only some minor changes in the gene expression after AgNP exposure. Nonetheless, as emerging evidence suggests lysosomal damage and autophagy dysfunction as critical mechanisms of NP-induced toxicity, future studies should also focus on these processes when considering NP toxicity (71). To investigate such mechanisms, Lysotracker, a cell-permeable fluorescent dye that selectively accumulates in acidic cellular compartments, such as lysosomes, can be used to visualize and quantify lysosomal content in live cells (86). As lysosomes are involved in autophagy, Lysotracker staining may offer insights into NP-induced disruptions of lysosomal function and downstream autophagic processes (71). Similarly, to investigate the effects of NPs on mitochondrial dynamics, fluorescent probes such as Mitotracker Red CMXRos and Mitotracker Green could be used to quantitatively assess the mitochondrial network morphology and function. Mitotracker Red CMXRos is a fluorescent probe that selectively accumulates in active mitochondria based on membrane potential. In contrast, Mitotracker

Green can accumulate in inactive mitochondria by binding to mitochondrial proteins. While this study used a qualitative TEM analysis to provide an initial impression of ultrastructural changes, the combined use of both dyes would allow researchers to obtain insights into mitochondrial morphology and the proportion of functionally active mitochondria. Future studies could integrate these methods to improve our understanding of NP-induced mitochondrial alterations (87, 88, 89).

A major strength of this study is the inclusion of multiple time points in both the gene expression analysis and the lipid droplet analysis, which enabled the assessment of cellular stress responses in a time-wise manner. This approach allows for the detection of both early and delayed cellular stress responses. Future studies should continue including multiple time points as this will be critical for identifying the temporal sequence of events, and ultimately, for constructing an adverse outcome pathway (AOP). This is a conceptual framework that describes causal linkages between a molecular initiating event, a sequence of intermediate key events, and the adverse outcome. AOPs play an important role in toxicological risk assessment because they provide a mechanistic basis for predicting toxicological outcomes. Moreover, they contribute to the development of alternative testing strategies by reducing the reliance on animal testing (90). Secondly, the use of hDPSCs presents another advantage. These MSCs are easily accessible, involving minimal ethical concerns. Furthermore, the comparative design, involving three widely encountered NPs, allowed for an evaluation of how NP type influences cellular responses. By focusing on ferroptosis, a recently discovered and still underexplored form of cell death, this study provides novel insights and adds relevance to the field of nanotoxicology. Finally, the development of an optimized Ferro Orange staining protocol further enhances the future applicability of this research.

Nonetheless, some limitations should also be acknowledged. First, the qualitative nature of the TEM analysis, based on a limited number of cells, restricts the strength of conclusions regarding organelle morphology. Second, for AgNPs and TiO_2NPs, only one particle size per NP type was investigated, limiting conclusions about size-dependent effects within the same material. Third, MDA levels were not measured following PSNP exposure due to time constraints, making it difficult to draw firm conclusions on lipid peroxidation, a hallmark of ferroptosis, for this NP type. Lastly, the sample sizes for the MDA and ORO stainings were limited. To strengthen the reliability of these findings, future studies should include larger sample sizes and repeated experiments. Together, this research highlights the complex interplay between NP characteristics like NP type and size, exposure time, and cellular stress responses.

CONCLUSION

This study investigated the effects of AgNPs, TiO_2NPs, and PSNPs on cellular stress responses in hDPSCs across multiple concentrations and time points. Results indicated particle-specific and size-dependent stress responses. In summary, AgNPs showed the strongest tendency toward inducing ferroptosis, marked by the differential expression of ferroptosis-related genes and increased lipid peroxidation. PSNPs triggered more moderate effects, with size-specific differences: the 1 µm particles induced stronger ferroptosis-related gene expression changes, while the 50 nm particles rather activated ER stress pathways. TiO_2NPs did not significantly induce ferroptosis but caused pronounced lipid droplet accumulation. Lipid droplet accumulation was observed across all NP types, likely through different mechanisms. These findings provide new insights into NP-induced cellular stress in stem cells, enhancing our understanding of NP-induced toxicity and supporting the need to consider both particle size and composition in the development of safer NPs.

REFERENCES

1. Najahi-Missaoui W, Arnold RD, Cummings BS. Safe Nanoparticles: Are We There Yet? Int J Mol Sci. 2020;22(1).
2. Gatoo MA, Naseem S, Arfat MY, Dar AM, Qasim K, Zubair S. Physicochemical properties of nanomaterials: implication in associated toxic manifestations. Biomed Res Int. 2014;2014:498420.
3. Ema M, Okuda H, Gamo M, Honda K. A review of reproductive and developmental toxicity of silver nanoparticles in laboratory animals. Reprod Toxicol. 2017;67:149-64.
4. Zhang J, Liu S, Han J, Wang Z, Zhang S. On the developmental toxicity of silver nanoparticles. Materials & Design. 2021;203:109611.
5. Giannandrea D, Parolini M, Citro V, De Felice B, Pezzotta A, Abazari N, et al. Nanoplastic impact on bone microenvironment: A snapshot from murine bone cells. Journal of Hazardous Materials. 2024;462:132717.
6. Presnell SC, Petersen B, Heidaran M. Stem cells in adult tissues. Seminars in Cell & Developmental Biology. 2002;13(5):369-76.
7. Ding D-C, Shyu W-C, Lin S-Z. Mesenchymal Stem Cells. Cell Transplantation. 2011;20(1):5-14.
8. Weatherbee BAT, Cui T, Zernicka-Goetz M. Modeling human embryo development with embryonic and extra-embryonic stem cells. Dev Biol. 2021;474:91-9.
9. Bassi A, Gough J, Zakikhani M, Downes S. 5 - Bone tissue regeneration. In: Bosworth LA, Downes S, editors. Electrospinning for Tissue Regeneration: Woodhead Publishing; 2011. p. 93-110.
10. Le H, Xu W, Zhuang X, Chang F, Wang Y, Ding J. Mesenchymal stem cells for cartilage regeneration. J Tissue Eng. 2020;11:2041731420943839.
11. Kangari P, Talaei-Khozani T, Razeghian-Jahromi I, Razmkhah M. Mesenchymal stem cells: amazing remedies for bone and cartilage defects. Stem Cell Research & Therapy. 2020;11(1):492.
12. Potdar PD, Jethmalani YD. Human dental pulp stem cells: Applications in future regenerative medicine. World J Stem Cells. 2015;7(5):839-51.
13. Ashri NY, Ajlan SA, Aldahmash AM. Dental pulp stem cells. Biology and use for periodontal tissue engineering. Saudi Med J. 2015;36(12):1391-9.
14. Wāng Y, Han Y, Xu D-X. Developmental impacts and toxicological hallmarks of silver nanoparticles across diverse biological models. Environmental Science and Ecotechnology. 2024;19:100325.
15. Gao X, Topping VD, Keltner Z, Sprando RL, Yourick JJ. Toxicity of nano- and ionic silver to embryonic stem cells: a comparative toxicogenomic study. Journal of Nanobiotechnology. 2017;15(1):31.
16. Liu F, Mahmood M, Xu Y, Watanabe F, Biris AS, Hansen DK, et al. Effects of silver nanoparticles on human and rat embryonic neural stem cells. Frontiers in Neuroscience. 2015;9.
17. Ahmad M, Khan MKA, Shahzad K, Ahmad N, Parveen M, Khan MS. Teratological effects of titanium dioxide nanoparticles in mice embryo. Environmental Science and Pollution Research. 2022;29(27):40724-33.
18. Noga M, Milan J, Frydrych A, Jurowski K. Toxicological Aspects, Safety Assessment, and Green Toxicology of Silver Nanoparticles (AgNPs)-Critical Review: State of the Art. Int J Mol Sci. 2023;24(6).
19. Kaushal A, Khurana I, Yadav P, Allawadhi P, Banothu AK, Neeradi D, et al. Advances in therapeutic applications of silver nanoparticles. Chemico-Biological Interactions. 2023;382:110590.

20. Skocaj M, Filipic M, Petkovic J, Novak S. Titanium dioxide in our everyday life; is it safe? Radiol Oncol. 2011;45(4):227-47.
21. Manzoor Q, Sajid A, Ali Z, Nazir A, Sajid A, Imtiaz F, et al. Toxicity spectrum and detrimental effects of titanium dioxide nanoparticles as an emerging pollutant: A review. Desalination and Water Treatment. 2024;317:100025.
22. Hu B, Cheng Z, Liang S. Advantages and prospects of stem cells in nanotoxicology. Chemosphere. 2022;291:132861.
23. Kik K, Bukowska B, Sicińska P. Polystyrene nanoparticles: Sources, occurrence in the environment, distribution in tissues, accumulation and toxicity to various organisms. Environmental Pollution. 2020;262:114297.
24. Waring RH, Harris RM, Mitchell SC. Plastic contamination of the food chain: A threat to human health? Maturitas. 2018;115:64-8.
25. Auta HS, Emenike CU, Fauziah SH. Distribution and importance of microplastics in the marine environment: A review of the sources, fate, effects, and potential solutions. Environment International. 2017;102:165-76.
26. Hernandez LM, Yousefi N, Tufenkji N. Are There Nanoplastics in Your Personal Care Products? Environmental Science & Technology Letters. 2017;4(7):280-5.
27. Hesler M, Aengenheister L, Ellinger B, Drexel R, Straskraba S, Jost C, et al. Multi-endpoint toxicological assessment of polystyrene nano- and microparticles in different biological models in vitro. Toxicology in Vitro. 2019;61:104610.
28. Chen J, Xu Z, Liu Y, Mei A, Wang X, Shi Q. Cellular absorption of polystyrene nanoplastics with different surface functionalization and the toxicity to RAW264.7 macrophage cells. Ecotoxicology and Environmental Safety. 2023;252:114574.
29. Champion JA, Mitragotri S. Role of target geometry in phagocytosis. Proc Natl Acad Sci U S A. 2006;103(13):4930-4.
30. Parupudi A, Mulagapati SHR, Subramony JA. Chapter 1 - Nanoparticle technologies: Recent state of the art and emerging opportunities. In: Kesharwani P, Singh KK, editors. Nanoparticle Therapeutics: Academic Press; 2022. p. 3-46.
31. Weiss M, Fan J, Claudel M, Sonntag T, Didier P, Ronzani C, et al. Density of surface charge is a more predictive factor of the toxicity of cationic carbon nanoparticles than zeta potential. J Nanobiotechnology. 2021;19(1):5.
32. Lu GW, Gao P. CHAPTER 3 - Emulsions and Microemulsions for Topical and Transdermal Drug Delivery. In: Kulkarni VS, editor. Handbook of Non-Invasive Drug Delivery Systems. Boston: William Andrew Publishing; 2010. p. 59-94.
33. Manke A, Wang L, Rojanasakul Y. Mechanisms of nanoparticle-induced oxidative stress and toxicity. Biomed Res Int. 2013;2013:942916.
34. Oberdörster G, Oberdörster E, Oberdörster J. Nanotoxicology: An Emerging Discipline Evolving from Studies of Ultrafine Particles. Environmental Health Perspectives. 2005;113(7):823-39.
35. Magdolenova Z, Collins A, Kumar A, Dhawan A, Stone V, Dusinska M. Mechanisms of genotoxicity. A review of in vitro and in vivo studies with engineered nanoparticles. Nanotoxicology. 2014;8(3):233-78.
36. Touyz RM. Molecular and cellular mechanisms in vascular injury in hypertension: role of angiotensin II. Curr Opin Nephrol Hypertens. 2005;14(2):125-31.
37. Mueller CF, Laude K, McNally JS, Harrison DG. ATVB in focus: redox mechanisms in blood vessels. Arterioscler Thromb Vasc Biol. 2005;25(2):274-8.

38. Halliwell B. Reactive species and antioxidants. Redox biology is a fundamental theme of aerobic life. Plant Physiol. 2006;141(2):312-22.
39. Sies H. Oxidative stress: oxidants and antioxidants. Experimental Physiology: Translation and Integration. 1997;82(2):291-5.
40. Huang CC, Aronstam RS, Chen DR, Huang YW. Oxidative stress, calcium homeostasis, and altered gene expression in human lung epithelial cells exposed to ZnO nanoparticles. Toxicol In Vitro. 2010;24(1):45-55.
41. Nel A, Xia T, Mädler L, Li N. Toxic potential of materials at the nanolevel. Science. 2006;311(5761):622-7.
42. Shvedova AA, Pietroiusti A, Fadeel B, Kagan VE. Mechanisms of carbon nanotube-induced toxicity: focus on oxidative stress. Toxicol Appl Pharmacol. 2012;261(2):121-33.
43. Li N, Xia T, Nel AE. The role of oxidative stress in ambient particulate matter-induced lung diseases and its implications in the toxicity of engineered nanoparticles. Free Radic Biol Med. 2008;44(9):1689-99.
44. Tang J, Lu X, Chen B, Cai E, Liu W, Jiang J, et al. Mechanisms of silver nanoparticles-induced cytotoxicity and apoptosis in rat tracheal epithelial cells. The Journal of Toxicological Sciences. 2019;44(3):155-65.
45. Ni H-M, Williams JA, Ding W-X. Mitochondrial dynamics and mitochondrial quality control. Redox biology. 2015;4:6-13.
46. Chen H, Chomyn A, Chan DC. Disruption of fusion results in mitochondrial heterogeneity and dysfunction. Journal of Biological Chemistry. 2005;280(28):26185-92.
47. Adebayo M, Singh S, Singh AP, Dasgupta S. Mitochondrial fusion and fission: The fine-tune balance for cellular homeostasis. Faseb j. 2021;35(6):e21620.
48. Hasnat M, Yuan Z, Naveed M, Khan A, Raza F, Xu D, et al. Drp1-associated mitochondrial dysfunction and mitochondrial autophagy: a novel mechanism in triptolide-induced hepatotoxicity. Cell Biology and Toxicology. 2019;35(3):267-80.
49. Bakare AB, Daniel J, Stabach J, Rojas A, Bell A, Henry B, et al. Quantifying Mitochondrial Dynamics in Patient Fibroblasts with Multiple Developmental Defects and Mitochondrial Disorders. International Journal of Molecular Sciences. 2021;22(12):6263.
50. Hou Y, Lai M, Chen X, Li J, Hu Y, Luo Z, et al. Effects of mesoporous SiO2, Fe3O4, and TiO2 nanoparticles on the biological functions of endothelial cells in vitro. Journal of Biomedical Materials Research Part A. 2014;102(6):1726-36.
51. Jia X, Wang S, Zhou L, Sun L. The Potential Liver, Brain, and Embryo Toxicity of Titanium Dioxide Nanoparticles on Mice. Nanoscale Research Letters. 2017;12(1):478.
52. Ostaszewska T, Śliwiński J, Kamaszewski M, Sysa P, Chojnacki M. Cytotoxicity of silver and copper nanoparticles on rainbow trout (Oncorhynchus mykiss) hepatocytes. Environmental Science and Pollution Research. 2018;25(1):908-15.
53. Pereira LC, Pazin M, Franco-Bernardes MF, Martins AdC, Barcelos GRM, Pereira MC, et al. A perspective of mitochondrial dysfunction in rats treated with silver and titanium nanoparticles (AgNPs and TiNPs). Journal of Trace Elements in Medicine and Biology. 2018;47:63-9.
54. Tong M, Saito T, Zhai P, Oka S-i, Mizushima W, Nakamura M, et al. Mitophagy is essential for maintaining cardiac function during high fat diet-induced diabetic cardiomyopathy. Circulation research. 2019;124(9):1360-71.
55. Schwarz DS, Blower MD. The endoplasmic reticulum: structure, function

and response to cellular signaling. Cell Mol Life Sci. 2016;73(1):79-94.
56. Cao Y, Long J, Liu L, He T, Jiang L, Zhao C, et al. A review of endoplasmic reticulum (ER) stress and nanoparticle (NP) exposure. Life Sci. 2017;186:33-42.
57. Hou C-C, Tsai T-L, Su W-P, Hsieh H-P, Yeh C-S, Shieh D-B, et al. Pronounced induction of endoplasmic reticulum stress and tumor suppression by surfactant-free poly(lactic-co-glycolic acid) nanoparticles via modulation of the PI3K signaling pathway. International Journal of Nanomedicine. 2013;8(null):2689-707.
58. Huo L, Chen R, Zhao L, Shi X, Bai R, Long D, et al. Silver nanoparticles activate endoplasmic reticulum stress signaling pathway in cell and mouse models: The role in toxicity evaluation. Biomaterials. 2015;61:307-15.
59. Mohamud R, Xiang SD, Selomulya C, Rolland JM, O'Hehir RE, Hardy CL, et al. The effects of engineered nanoparticles on pulmonary immune homeostasis. Drug Metab Rev. 2014;46(2):176-90.
60. Dąbrowska-Bouta B, Sulkowski G, Gewartowska M, Strużyńska L. Endoplasmic Reticulum Stress Underlies Nanosilver-Induced Neurotoxicity in Immature Rat Brain. Int J Mol Sci. 2022;23(21).
61. Zheng G, Zhang J, Zhang X, Zhang Z, Liu S, Zhang S, et al. Implications of ferroptosis in silver nanoparticle-induced cytotoxicity of macrophages. Ecotoxicology and Environmental Safety. 2023;259:115057.
62. Xie Y, Hou W, Song X, Yu Y, Huang J, Sun X, et al. Ferroptosis: process and function. Cell Death & Differentiation. 2016;23(3):369-79.
63. Liu M, Liu B, Liu Q, Du K, Wang Z, He N. Nanomaterial-induced ferroptosis for cancer specific therapy. Coordination Chemistry Reviews. 2019;382:160-80.
64. Hassannia B, Vandenabeele P, Vanden Berghe T. Targeting Ferroptosis to Iron Out Cancer. Cancer Cell. 2019;35(6):830-49.
65. Ahsan H, Hasan MY, Ahmad R. Chapter 2 - Ferroptosis: Oxidative stress and pathophysiology. In: Maurya PK, Qamar I, editors. Novel Therapeutic Approaches Targeting Oxidative Stress: Academic Press; 2022. p. 19-26.
66. Yang Wan S, SriRamaratnam R, Welsch Matthew E, Shimada K, Skouta R, Viswanathan Vasanthi S, et al. Regulation of Ferroptotic Cancer Cell Death by GPX4. Cell. 2014;156(1):317-31.
67. Yu Y, Yan Y, Niu F, Wang Y, Chen X, Su G, et al. Ferroptosis: a cell death connecting oxidative stress, inflammation and cardiovascular diseases. Cell Death Discovery. 2021;7(1):193.
68. Yang WS, SriRamaratnam R, Welsch ME, Shimada K, Skouta R, Viswanathan VS, et al. Regulation of ferroptotic cancer cell death by GPX4. Cell. 2014;156(1-2):317-31.
69. Zhang Y, Hales BF, Robaire B. Exposure to polystyrene nanoplastics induces lysosomal enlargement and lipid droplet accumulation in KGN human ovarian granulosa cells. Archives of Toxicology. 2025.
70. Medici S, Peana M, Pelucelli A, Zoroddu MA. An updated overview on metal nanoparticles toxicity. Seminars in Cancer Biology. 2021;76:17-26.
71. Feng Y, Fu H, Zhang X, Liu S, Wei X. Lysosome toxicities induced by nanoparticle exposure and related mechanisms. Ecotoxicology and Environmental Safety. 2024;286:117215.
72. Abulikemu A, Zhao X, Qi Y, Liu Y, Wang J, Zhou W, et al. Lysosomal impairment-mediated autophagy dysfunction responsible for the vascular endothelial apoptosis caused by silica nanoparticle via ROS/PARP1/AIF signaling pathway. Environmental Pollution. 2022;304:119202.
73. Zhai X, Yan W, Liu S, Tian L, Zhang Y, Zhao Y, et al. Silver nanoparticles induce

iron accumulation-associated cognitive impairment via modulating neuronal ferroptosis. Environmental Pollution. 2024;346:123555.
74. Ayala A, Muñoz MF, Argüelles S. Lipid peroxidation: production, metabolism, and signaling mechanisms of malondialdehyde and 4-hydroxy-2-nonenal. Oxid Med Cell Longev. 2014;2014:360438.
75. Mühlfeld C, Rothen-Rutishauser B, Vanhecke D, Blank F, Gehr P, Ochs M. Visualization and quantitative analysis of nanoparticles in the respiratory tract by transmission electron microscopy. Part Fibre Toxicol. 2007;4:11.
76. Mandarim-de-Lacerda CA, del-Sol M. Tips for Studies with Quantitative Morphology (Morphometry and Stereology). International Journal of Morphology. 2017;35:1482-94.
77. Bailey AP, Koster G, Guillermier C, Hirst EM, MacRae JI, Lechene CP, et al. Antioxidant Role for Lipid Droplets in a Stem Cell Niche of Drosophila. Cell. 2015;163(2):340-53.
78. Bai Y, Meng L, Han L, Jia Y, Zhao Y, Gao H, et al. Lipid storage and lipophagy regulates ferroptosis. Biochemical and Biophysical Research Communications. 2019;508(4):997-1003.
79. Li B, Zhang T, Tang M. Toxicity mechanism of nanomaterials: Focus on endoplasmic reticulum stress. Science of The Total Environment. 2022;834:155417.
80. Jin X, Tang J, Qiu X, Nie X, Ou S, Wu G, et al. Ferroptosis: Emerging mechanisms, biological function, and therapeutic potential in cancer and inflammation. Cell Death Discovery. 2024;10(1):45.
81. Huang F, Feng Y, Wang Z-A, Cao Y, Yan Q, Wang W, et al. Environmentally Relevant Concentrations of Commercial Titanium Dioxide Nanoparticles Induce Ferroptosis in HUVECs. Environmental Toxicology.n/a(n/a).
82. Jarc E, Petan T. Lipid Droplets and the Management of Cellular Stress. Yale J Biol Med. 2019;92(3):435-52.
83. Xiong S, George S, Ji Z, Lin S, Yu H, Damoiseaux R, et al. Size of TiO(2) nanoparticles influences their phototoxicity: an in vitro investigation. Arch Toxicol. 2013;87(1):99-109.
84. Wu Q, Liu C, Liu D, Wang Y, Qi H, Liu X, et al. Polystyrene nanoplastics-induced lung apoptosis and ferroptosis via ROS-dependent endoplasmic reticulum stress. Science of The Total Environment. 2024;912:169260.
85. Li J, Jia YC, Ding YX, Bai J, Cao F, Li F. The crosstalk between ferroptosis and mitochondrial dynamic regulatory networks. Int J Biol Sci. 2023;19(9):2756-71.
86. Neun BW, Stern ST. Monitoring Lysosomal Activity in Nanoparticle-Treated Cells. In: McNeil SE, editor. Characterization of Nanoparticles Intended for Drug Delivery. Totowa, NJ: Humana Press; 2011. p. 207-12.
87. Li J, Zhang B, Chang X, Gan J, Li W, Niu S, et al. Silver nanoparticles modulate mitochondrial dynamics and biogenesis in HepG2 cells. Environmental Pollution. 2020;256:113430.
88. Pendergrass W, Wolf N, Poot M. Efficacy of MitoTracker Green™ and CMXrosamine to measure changes in mitochondrial membrane potentials in living cells and tissues. Cytometry Part A. 2004;61A(2):162-9.
89. Neikirk K, Marshall AG, Kula B, Smith N, LeBlanc S, Hinton A. MitoTracker: A useful tool in need of better alternatives. European Journal of Cell Biology. 2023;102(4):151371.
90. Halappanavar S, van den Brule S, Nymark P, Gaté L, Seidel C, Valentino S, et al. Adverse outcome pathways as a tool for the design of testing strategies to support the safety assessment of emerging advanced materials at the nanoscale. Particle and Fibre Toxicology. 2020;17(1):16.

Acknowledgements – First of all, I would like to thank Prof. Dr. Karen Smeets for giving me the opportunity to work in her research group. I would also like to thank my supervisor, Ms. Anke Huysmans, for her guidance during the internship period and the feedback that I received during the writing process. Ms. Ines Tejeda and Prof. Dr. Nelly Saenen are thanked for their technical assistance. Additionally, I would like to thank Ms. Natascha Steffanie for her technical assistance. Finally, Anneleen Peeters and Reja Trippaers are sincerely thanked for their support in the lab.

Author contributions – KS and AH conceived and designed the research. AH and LR performed experiments and data analysis. LR wrote the paper. All authors carefully edited the manuscript.

This text was grammatically supported by GenAI.

SUPPLEMENTARY INFORMATION

Supplementary Table 1 – Information on selected genes and primers

Gene (pathway)	Forward primer (5'-3')	Reverse primer (5'-3')
Ferroptosis		
TFRC	GCTGGAGACTTTGGATCGGTTGG	TATACAACAGTGGGCTGGCAGAAAC
PTGS2	TTGCTGGCAGGGTTGCTGGTGGTA	CATCTGCCTGCTCTGGTCAATCGAA
SLC7A11	CTCCAGGTTATTCTATGTTGCGTCT	CAAAGGGTGCAAAACAATAACAGC
GPX4	GCC TTC CCG TGT AAC CAG TT	TTC ATC CAC TTC CAC AGC GG
HMOX1	CTGCTCAACATCCAGCTCTTTG	CTCCACGGGGGCAGAATCTT
ER stress		
XBP1s	CTGAGTCCGAATCAGGTGCAG	ATCCATGGGGAGATGTTCTGG
XBP1u	CAGCACTCAGACTACGTGCA	ATCCATGGGGAGATGTTCTGG
CHOP	AGAACCAGGAAACGGAAACAGA	TCTCCTTCATGCGCTGCTTT
ATF4	ATG ACC GAA ATG AGC TTC CTG	GCT GGA GAA CCC ATG AGG T
PDIA4	TTGTTGGCGTAGATTTGGCT	TGCTCAGTGGCAGCTCTCAC
Mitochondrial dynamics		
MFF	AAC CCC TGG CAC TGA AAA CA	TGA GGG GTT GTA GGA GGT CT
FIS	AGA TGG ACT CGT GGG CAT GG	ACA GGG AAA GGA CAG CGA GG
P53	GAT TTG ATG CTG TCC CCG GA	CTG GCA TTC TGG GAG CTT CA
MFN1	CCT TTT ACC TCA GCC TCC CA	CAG ACC CAA GGA TCC ACA CT
Autophagy		
ATG14	CAATCGAGGAAGTAAAGACGG	TCGTCCTGAGAGGTAAGTTG
ATG7	TGAGTTGACCCAGAAGAAGCT	CCCAGCAGAGTCACCATTGT
NBR1	GGTATCCATCAACAGTCAAGG	CGTTTTGCTCCTACAACTGG
ULK1	ACAAGAAGAACCTCGCCAAG	TTCCTTCAGGATTTTGATTTCC
WDR45	CCTTATTCGCCTCTTTGACAC	GCAAAGATATGGACAGTACCC
Reference gene		
GAPDH	TGT TCG TCA TGG GTG TGA AC	ATG GCA TGG ACT GTG GTC AT
HPRT1	CCTGGCGTCGTGATTAGTGA	CGAGCAAGACGTTCAGTCCT
TBP	CAC GAA CCA CGG CAC TGA TT	TTT TCT TGC TGC CAG TCT GGA C
RPLP0	CGTCCTCGTGGAAGTGACAT	TAGTTGGACTTCCAGGTCGC

Supplementary experimental procedure 1- Optimization of Ferro Orange staining

Ferroptosis, an iron-driven non-apoptotic cell death, is characterized by intracellular iron accumulation. To measure intracellular ferrous iron (Fe^{2+}) levels, Ferro Orange (FO), a fluorescent probe that specifically binds to Fe^{2+}, was utilized. The optimization process aimed to refine the protocol for Ferro Orange staining and improve image quality through systematic adjustments.

Initial Protocol Design

The optimization process began by culturing cells in 8-well IBIDI chamber slides at a seeding density of 2 x 10^4 cells per well, followed by a 48-hour growing period. One of the goals was to compare two different media, DPBS and phenol-free Dulbecco's Modified Eagle Medium (DMEM, Gibco, Fisher Scientific, Brussels, Belgium), to evaluate their influence on background fluorescence and signal quality. For each medium, a positive control (100 µM $Fe(NH_4)_2(SO_4)_2$, Honeywell Fluka, Charlotte, North Carolina, USA) and a negative control were included. After washing the cells once with the respective medium, the positive control was incubated for 30 minutes at 37°C with the iron solution. Then, cells were washed three times with their respective medium and stained with 1 µM FO (Cell Signaling Technology, Danvers, Massachusetts, USA). The cells were incubated with the probe for 30 minutes at 37°C. Confocal laser microscopy was performed at an emission wavelength of 574 nm. At 10x magnification, the fluorescence signal was acceptable. On the other hand, at 20x magnification, increased background noise was observed (Supplementary Figure 1), particularly in DMEM-treated wells. In contrast, DPBS-treated wells showed a clearer signal, suggesting that DPBS is more suitable for FO staining.

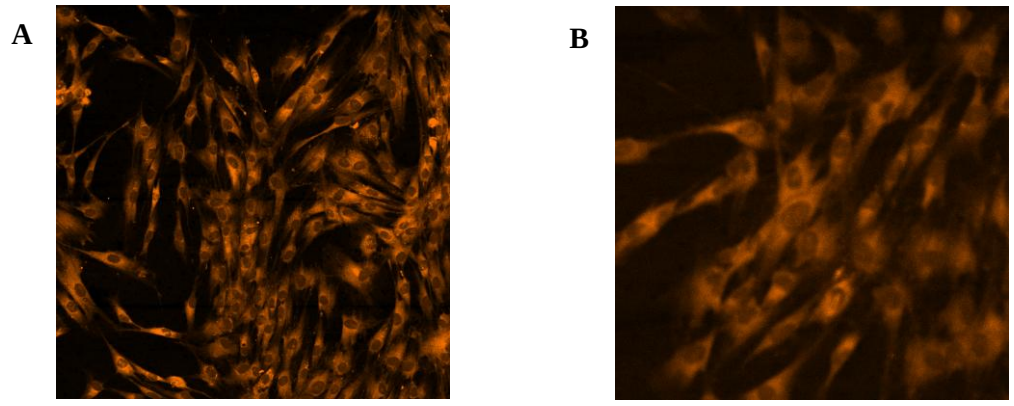

Supplementary Figure 1 – Confocal laser microscopy images of FO, addition of 100µM $Fe(NH_4)_2(SO_4)_2$ was used as a positive control. (A) Positive control in DPBS imaged at 10x magnification, (B) Positive control in DPBS imaged at 20x magnification.

Extended Incubation Time

To confirm that DPBS yielded less background noise and to assess whether a longer incubation time could enhance the signal intensity, the experiment was repeated with an extended incubation time of 1 hour with FO. Again, DPBS-treated cells consistently exhibited lower background noise compared to those treated with DMEM (Supplementary Figure 2). Based on this observation, further experiments were carried out using DPBS to ensure clearer imaging with minimal interference.

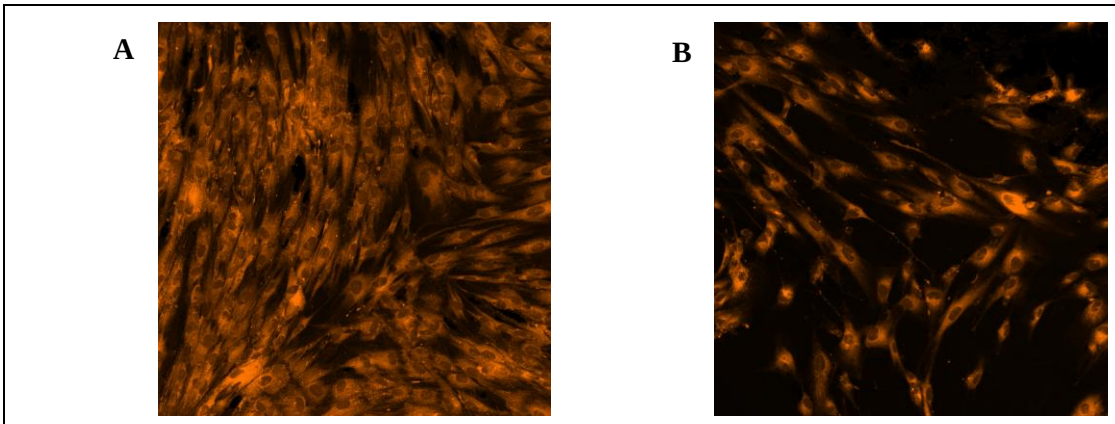

Supplementary Figure 2 – Confocal laser microscopy images of FO, addition of 100µM $Fe(NH_4)_2(SO_4)_2$ was used as a positive control. (A) Positive control in DPBS imaged at 10x magnification, (B) Positive control in DMEM imaged at 10x magnification.

Optimization of Ferro Orange Concentration and Cell Permeabilization

Next, to improve the fluorescence signal, the concentration of Ferro Orange was increased to 3 µM. Additionally, digitonin, a cell-permeabilizing agent, was introduced to increase the probe's access to intracellular iron. Before adding Ferro Orange, the cells were washed with warm DPBS and incubated with digitonin (10 µM and 20µM in DPBS) for 10 minutes at RT. Following this step, the cells were washed again, and the Ferro Orange staining procedure was continued as previously described. However, these concentrations caused extensive cell death.

Optimization of Digitonin Concentration

To determine a concentration that permits sufficient membrane permeabilization while maintaining viability, a range of digitonin concentrations (10 µM, 5 µM, 3 µM, and 1 µM) was tested. Trypan blue staining was used to assess membrane permeability. At 10 and 5 µM, cells detached rapidly, whereas 3 µM allowed cells to remain adherent for up to 30 minutes. 1 µM showed the most favorable scenario, with minimal cell detachment even after 1 hour. Additionally, after 45 minutes, an increased trypan blue penetration was observed, confirming the effectiveness of trypan blue as a cell permeabilizer. This concentration was selected for further optimization steps.

Optimization of Positive Control Concentration

Although several improvements had been made to the staining protocol, including the use of DPBS to reduce background fluorescence, an extended incubation time to increase signal intensity, and the optimization of digitonin concentration to enhance cell permeability, the difference in signal intensity between the positive and negative controls remained minimal when using 1µM of digitonin and 100 µM $Fe(NH_4)_2(SO_4)_2$. To address this, higher concentrations of the positive control were tested: 200 µM, 500 µM, and 1 mM. Increasing the iron concentration significantly enhanced the fluorescence signal: negative control (47.62 ±1.18 a.u.), 200 µM (69.86±1.95 a.u), 500 µM (73.17±2.16 a.u.), and 1 mM (55.82±3.11 a.u.). Notably, 500 µM $Fe(NH_4)_2(SO_4)_2$ yielded the strongest and most consistent signal with clear differentiation between controls (Supplementary Figure 3). At 1 mM $Fe(NH_4)_2(SO_4)_2$, a drop in signal quality was observed, possibly due to cellular toxicity at this high iron load.

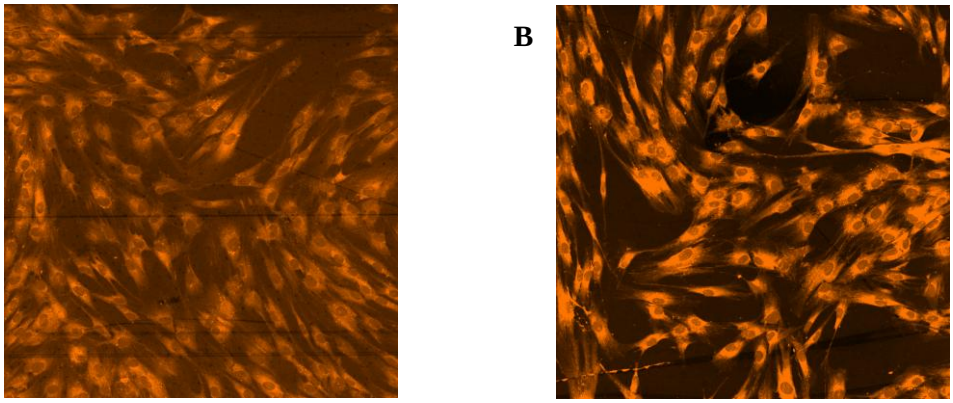

Supplementary Figure 3 – Confocal laser microscopy images of FO, addition of 500µM $Fe(NH_4)_2(SO_4)_2$ was used as a positive control. (A) negative control in DPBS with 1 µM of digitonin imaged at 10x magnification, (B) Positive control in DPBS with 1 µM of digitonin imaged at 10x magnification.

Final optimized protocol

Through iterative optimization, the protocol was refined to enhance both cell viability and the quality of Ferro Orange staining. Key changes included the use of DPBS to minimize background signal, the identification of an optimal digitonin concentration (1 µM) to balance cell permeabilization and survival, and the adjustment of positive control concentrations to achieve a more distinct signal. In the final optimized protocol, DPSCs were seeded in an 8-well IBIDI chamber slide at a density of 2 x 10^4 cells/well and cultured for 48 hours. After washing the cells once with warm DPBS, 1 µM digitonin was added to permeabilize the cell membranes. For the positive control, cells were treated with 1 µM digitonin in combination with 500 µM. Both negative and positive controls were incubated for 30 minutes at 37 °C. Then, cells were washed three times with DPBS, 1 µM of FO was added, and cells were incubated for 30 minutes at 37°C. Finally, the cells were imaged using confocal laser microscopy at an emission wavelength of 574 nm.